Integrated Computational Materials Engineering to Predict Melt-Pool Dimensions and 3D Grain Structures for Selective Laser Melting of Inconel 625

Jonathan Robichaud[1] · Tim Vincent[1] · Ben Schultheis[1] · Anil Chaudhary[1]

Abstract

This work presents a comparison of simulation results with the experimental data for four of the six challenges within the National Institute of Standards and Technology (NIST) Additive Manufacturing (AM) Benchmark Test Series (AM Bench) problem AMB2018-02. This comparison is akin to a test case to assess the technology maturity level (TML) for the AM predictive capabilities that can be utilized to improve AM products in the industry. The solutions are for the prediction of melt-pool geometry, cooling rate, solidification grain shapes, and their 3D structure. These results were obtained using the Additive Manufacturing Parameter Predictor (AMP^2) software. AMP^2 is an Integrated Computational Materials Engineering (ICME) suite of software developed by Applied Optimization, Inc. (AO). The melt-pool geometry is obtained using a thermal-computational fluid dynamics (CFD) solution of melt-pool physics. The melt-pool geometry, mean track cross section, 3D distribution of thermal gradient, and the liquid-to-solid interface velocity are predicted by the thermal-CFD model and utilized as input for the solidification grain structure computation. The grain shapes and 3D structure are modeled using cellular automata (CA). AO received a second-place award for predicting the grain structure within three single laser tracks on a bare plate of alloy Inconel 625 (IN625).

Keywords Integrated computational materials engineering · Additive manufacturing · Computational fluid dynamics · Cellular automata · Inconel 625

Introduction

Three salient aspects of the systems engineering process for the technology transition of simulation methods within the Department of Defense (DoD) are the evaluation of its cost, feasibility, and technology maturity level (TML) [1, 2]. This paper presents a test case, which is akin to an assessment of TML for AM predictive capability within small- to medium-sized industrial environments. The results presented in this paper comprise an outcome of blind tests performed using the material data available in open literature, off-the-shelf simulation software, and the experimental data provided by the National Institute of Standards and Technology (NIST) for Additive Manufacturing (AM) Benchmark Test Series (AM Bench) problem AMB2018-02.

Benchmark problem AMB2018-02 consists of modeling a series of single scan tracks on a bare metal substrate of alloy Inconel 625 (IN625). The scope of this modeling challenge is the prediction of melt-pool cross section, length and temperature characteristics, solidification microstructure, and 3D topography of the solidified tracks.

The prediction of melt-pool geometry, temperature distribution, and solidification microstructure was performed using the Additive Manufacturing Parameter Predictor (AMP^2) software developed by Applied Optimization, Inc. (AO) [3]. AMP^2 is an Integrated Computational Materials Engineering (ICME) suite of software capable of performing multi-scale analysis of the additive manufacturing (AM) process, which zooms in on the detailed material behavior at defined points of interest. The multi-scale analysis procedure comprises three levels of refinement: macro-, meso-, and micro-scales. The analytical methods in AMP^2 are developed based upon a rich pedigree of AM research reported in the technical literature for the simulation of high-temperature material behavior, thermal-fluid flow, vaporization, rapid solidification, and microstructure evolution [4–9]. A major challenge in the industrial

✉ Anil Chaudhary
anil@appliedo.com

1 Applied Optimization, 3040 Presidential Dr Suite 100, Fairborn, OH 45324, USA

utilization of these analytical methods is the insufficiency of high-temperature material properties and experimental data as well as the time and effort required to assess the fidelity of predictions versus only performing experimental trials (i.e., TML > 2). Since a direct comparison of one implementation of AM predictive methods versus another is difficult for a single organization, the AM-Bench provides a neutral forum for such an evaluation [10].

The macro-scale analysis in AMP^2 is performed at the part scale on a layer-by-layer basis to predict the heat buildup and the part distortion. The meso-scale analysis is performed at the scale of an individual layer where one or more points of interest reside, and it computes the build temperature distribution as a function of the scan strategy. The micro-scale analysis is performed at the scale of single or multiple tracks to predict the melt-pool physics at the points of interest. Its results are utilized to assess the propensity of build defects and to down select the processing parameters. The micro-scale analysis is performed using ParaGen software developed by AO. ParaGen is a software application within AMP^2. It automates the melt-pool physics simulations, and its output serves as an input for the modeling of solidification microstructure and solid-state transformations in the as-deposited layers of material.

The results reported in this paper were obtained using a two-step approach as follows:

1. Predict melt-pool geometry: The prediction of melt-pool geometry as a function of the laser scan parameters was performed using the ParaGen software. Since the laser scan tracks were made on bare metal, the macro- and meso-scale analyses in AMP^2 were not required. From the simulation results, the melt-pool geometries and the 3D temperature distributions were extracted and utilized as inputs for microstructure predictions.
2. Predict solidification microstructures: The thermal data from the melt-pool simulation was utilized in order to predict the 3D geometry of the liquid-to-solid interface

locations, and the thermal gradient (G) and the liquid-to-solid interface velocity (R). The dendrite tip temperature was calculated using the interface response function theory [9]. The 3D geometry of the liquid-to-solid interface and the G and R parameter data were provided as input to a cellular automata (CA) code developed by AO (CA-Solidification) to predict the evolution of the solidification grain structure.

Melt-Pool Simulation

The melt-pool simulation is the third step of the multi-scale simulation procedure in AMP^2 (Fig. 1). The macro- and meso-scale simulations are on a length scale of millimeters. The micro-scale melt-pool simulation is on a length scale of ~ 10* (melt-pool length). Since the melt-pool length is unknown a priori, the micro-scale length scale is set automatically by the iterative solution, which computes the melt-pool dimensions. The thermal boundary conditions for the melt-pool simulation at a given location are generated from the macro- and meso-scale simulations. Although the temperature distribution at the part and layer scale is non-uniform, the thermal boundary conditions for the melt-pool simulation are assumed to be steady state, corresponding to the temperature distribution on a plane perpendicular to the longitudinal axis of the laser track at the location of interest. In Fig. 1, such a plane would be a radial cross section through the wall of the part. Accordingly, the melt-pool thermal-CFD simulation solves the incompressible Navier-Stokes equations and the thermal energy equation with a solid–liquid phase change for steady-state melt-pool physics. The simulation uses inputs of material property data and AM process setup parameters to perform detailed parametric analyses. From the numerical analysis, the melt-pool geometry, flow field, and temperature distribution are predicted.

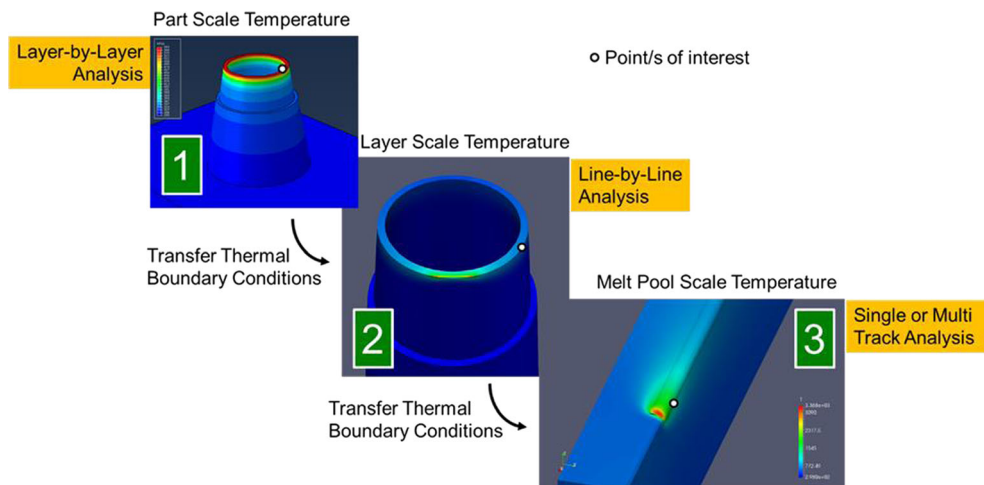Fig. 1 Illustration of multi-scale simulation procedure in AMP^2 [3]

Table 1 Other thermal material properties of IN625

Material property	Value
Latent heat (J kg^{-1}) [16]	2.27e5
Vaporization heat (J kg^{-1})*	6.40e6
Solidus temperature (K)	1563
Liquidus temperature (K)	1623
Boiling temperature (K)*	3188
Solid emissivity* [17]	0.53
Liquid emissivity* [17]	0.41
Laser absorptance [18]	0.51
Viscosity (kg m^{-1} s^{-1})	6.14e−7
Gradient of surface tension with respect to temperature (N m^{-1} K^{-1})*	− 1.10e−4
Reference value for surface tension (σ_0 (N m^{-1}))*	1.842
Reference temperature (T_0 (K))*	1998

The melt-pool cross-section geometry and length are computed iteratively such that the thermal and fluid flow equilibrium conditions are fulfilled.

The thermal-CFD melt-pool solution accounts for the effects of phase change, heat of fusion, and heat of vaporization. It uses a Eulerian, steady-state, CFD solver to simulate melt-pool shape, temperature, and fluid flow [11]. Equations (1), (2), and (3) are utilized to model the conservation of mass, momentum, and energy, respectively.

$$\frac{\partial(\rho u_j)}{\partial x_j} = 0 \quad (1)$$

$$\frac{\partial \rho u_j u_i}{\partial x_j} = -\frac{\partial p}{\partial x_i} - gh_d\frac{\partial \rho}{\partial x_i} + \frac{\partial}{\partial x_j}\left[\mu\left(\frac{\partial u_i}{\partial x_j} + \frac{\partial u_j}{\partial x_i} - \frac{2}{3}\frac{\partial u_k}{\partial x_k}\delta_{ij}\right)\right] + D_c(V_i - u_i) \quad (2)$$

$$\rho c_p u_j \frac{\partial T}{\partial x_j} = \frac{\partial}{\partial x_j}\left[k\frac{\partial T}{\partial x_j}\right] - \rho H_f\left(u_j\frac{\partial \alpha}{\partial x_j}\right) + \dot{Q}_L + \dot{Q}_E \quad (3)$$

where, u_i is liquid velocity, V_i is the laser scan velocity, x_i is the Cartesian coordinate, T is temperature, δ_{ij} is the Kronecker delta, p is the dynamic pressure (total minus hydrostatic pressure), μ is the dynamic viscosity, H_f is latent heat of fusion, g is the gravitational constant, h_d is the depth from the top surface of the melt pool, c_p is specific heat, k is thermal conductivity, and ρ is density. D_c is the D'arcy type phase coefficient which is used to switch between constant velocity in the solid and momentum conservation in the liquid. α is the phase fraction and equal to 0 in the solid region and 1 in the liquid region. The last two terms in Eq. (3) represent the laser energy absorption ($\dot{Q}_L$) and the energy lost to evaporation ($\dot{Q}_E$). The rate of material evaporation is computed using a scaled form of the Langmuir equation [12]:

$$J_v = \sum_i \frac{2}{15} a_i P_i^o \sqrt{M_i/T} \quad (4)$$

where a_i is the activity of element i in the liquid alloy, P_i^o is the equilibrium vapor pressure of element i over pure liquid at temperature T, and M_i is the molecular weight of element i. To calculate P_i^o, the Clausius-Clapeyron equation is used as follows:

$$P_i^o = P_{ATM}\exp\left(\left(\frac{1}{T_{boil}} - \frac{1}{T}\right)\frac{H_{v,i}M_i}{R}\right) \quad (5)$$
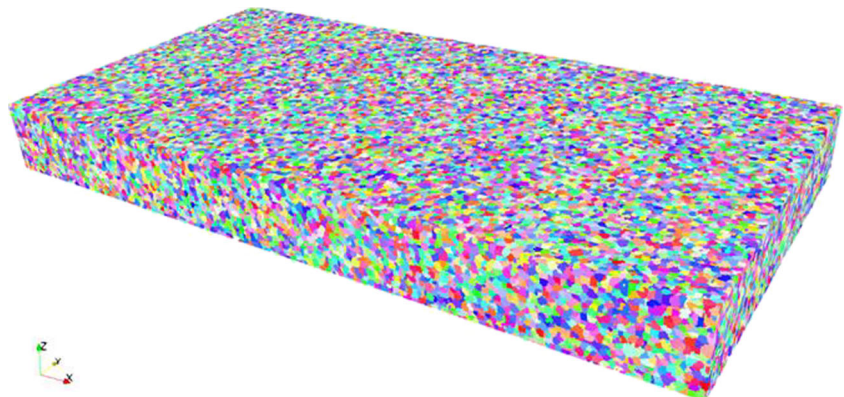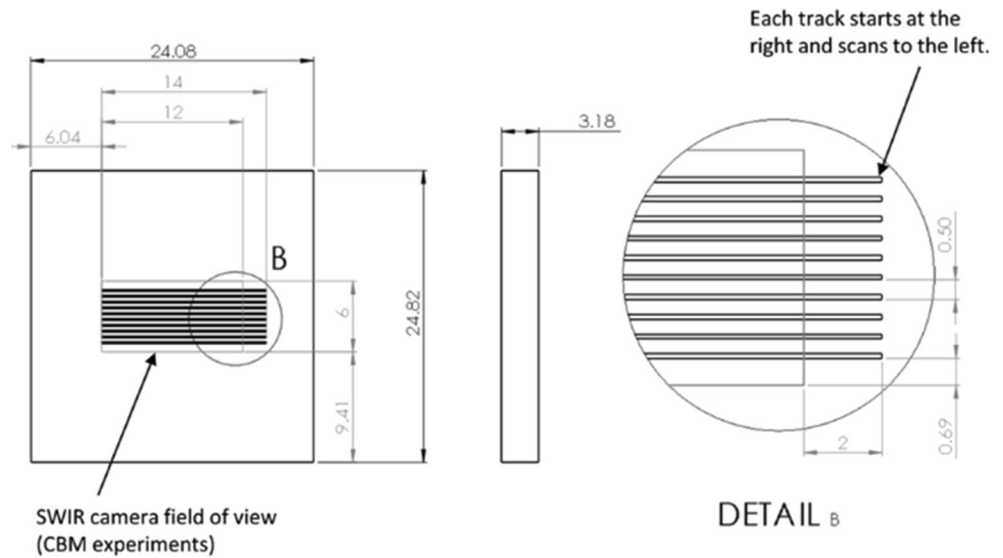
Fig. 2 Initial substrate generated with DREAM.3D software [19]

Fig. 3 Schematic of the substrate with all ten tracks [21] with the dimensions in millimeters

Each track starts at the right and scans to the left.

DETAIL B

SWIR camera field of view (CBM experiments)

where P_{ATM} is the ambient pressure, T_{boil} is the boiling temperature, $H_{v, i}$ is the enthalpy of vaporization for the element i, and R is the universal gas constant. The rate of mass loss (J_v) is used to compute a rate of energy loss due to evaporation as follows:

$$\dot{Q}_E = J_v(H_v + c_p T) \tag{6}$$

where H_v is the enthalpy of evaporation for the alloy. The Marangoni shear stress at the gas-liquid interface is modeled using Eqs. (7) and (8):

$$u_i \hat{n}_i = V_j \hat{n}_j \tag{7}$$

$$\frac{\partial(u_i - u_j \hat{n}_j \hat{n}_i)}{\partial x_j} \hat{n}_j = \frac{\alpha}{\mu} \frac{d\gamma}{dT} \left(\frac{\partial T}{\partial x_i} - \hat{n}_i \left(\hat{n}_j \frac{\partial T}{\partial x_j} \right) \right) \tag{8}$$

where $\hat{n}_i$ is the normal vector at the gas-liquid interface boundary and $\frac{d\gamma}{dT}$ is the derivative of surface tension with respect to temperature. The thermal-CFD solver uses a pressure-corrector formulation to solve the incompressible conservation equations. Accordingly, the out-flow faces are set to zero-gauge pressure, and all other faces are assigned a zero-pressure gradient in the direction of the surface normal, or:

$$p = 0 \text{ on the out-flow faces} \tag{9}$$

$$\frac{\partial p}{\partial x_j} \hat{n}_j = 0 \text{ elsewhere} \tag{10}$$

Table 2 Process parameters for each case

| Case	Laser power (W)	Scan speed (m s^{-1})
A	150	0.4
B	195	0.8
C	195	1.2

Related Work on the Assessment of Accuracy for Melt-Pool Predictions

A comparison of the predictions of melt-pool dimensions with the experimental work reported by Heigel and Lane [13] and Criales et al. [14] is given in Appendixes 1 and 2. The experimental data includes the melt-pool geometry for scan passes on a bare plate as well as with powder recoat for alloy IN625 for laser power ranging from 49 to 195 W and scan speed between 200 and 875 mm/s. The thermophysical properties of IN625 were obtained from Capriccioli and Frosi [15]. Table 1 contains the remaining material properties with the corresponding reference citations. Material properties with asterisks in Table 1 are data reported for alloy IN718 and are thus approximate values for alloy IN625.

Criales et al. [14] studied the powder bed scan passes; the width and depth of the melt pool were measured. These experiments consisted of multiple tracks alternating scan direction, which resulted in higher substrate temperature at the beginning of subsequent tracks. The melt-pool width and depth were measured close to the end of the substrate, which provided two distinct melt-pool dimensions. For a cooler substrate, the simulations had an average error of 4% and 18% for the prediction of width and depth, respectively. For the subsequent track where the substrate was at higher temperature, the simulations had an average error of 18% and 24% for width and depth, respectively.

The scan passes on a bare plate were performed by Heigel and Lane [13]; the length was measured experimentally, and the simulation predictions had an error ranging from 5 to 65%. We observed that for higher laser power, the error percentage was larger.

Fig. 4 Schematic of the cooling rate definition [21]

$$\text{Cooling rate} = \frac{dT}{dt} = \frac{1290 - 1000}{(d2 - d1)/V}$$
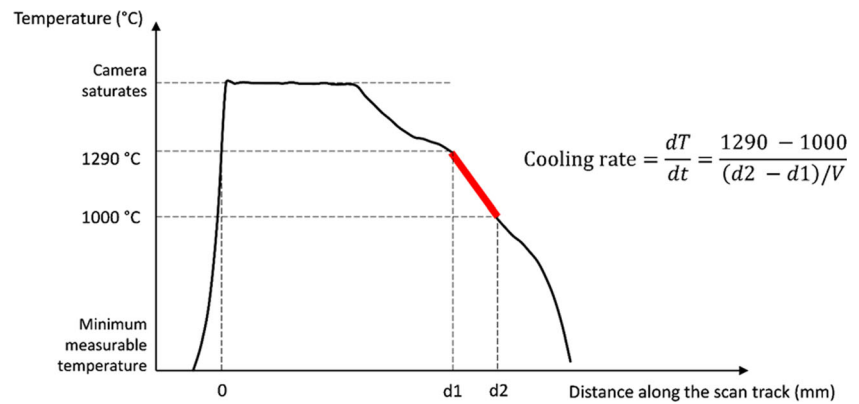
Solidification Grain Structure Simulation

The solidification grain structure simulation was performed using the CA-Solidification software developed by AO. This software uses the temperature and melt-pool dimension data generated by the melt-pool simulation as input. It uses a 3D uniform discretization to represent the CA grid (Fig. 2). At the start of simulation, each cell in the CA grid is initialized with a random distribution of grain size and crystal orientation using the DREAM.3D software [19]. Then, for each track in the simulation, the melt-pool thermal profile from the melt-pool simulation is mapped onto the CA grid. Next, the solidification grain structure is updated based on the melt-pool solidification front parameters as it moves through the CA grid.

The CA growth rules for the CA grid cells define the process for the growth of solidification grain structures. These rules utilize the growth model from Rai et al. [20]. This growth model considers that there is a "grain envelope" at the center of each CA cell, which emulates the dendrite arms. The salient steps for the CA calculation using this model are as follows: (1) At each time step, the grain envelopes are considered to grow in the epitaxial direction. (2) The solid cells on the solid-liquid interface are grown based on the simulation time step, easy growth directions, and the dendrite tip velocity which is computed as a function of the melt-pool geometry and the liquid-to-solid interface velocity. (3) Next, the liquid cells are considered to become solid with the orientation of the neighboring cell that has grown the furthest into the liquid cell. If no neighboring growing cells have sufficiently grown
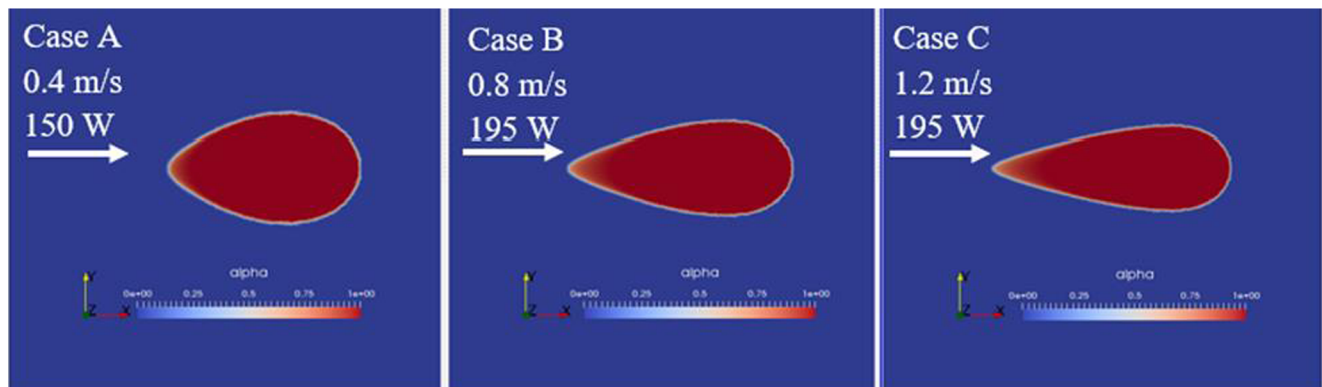
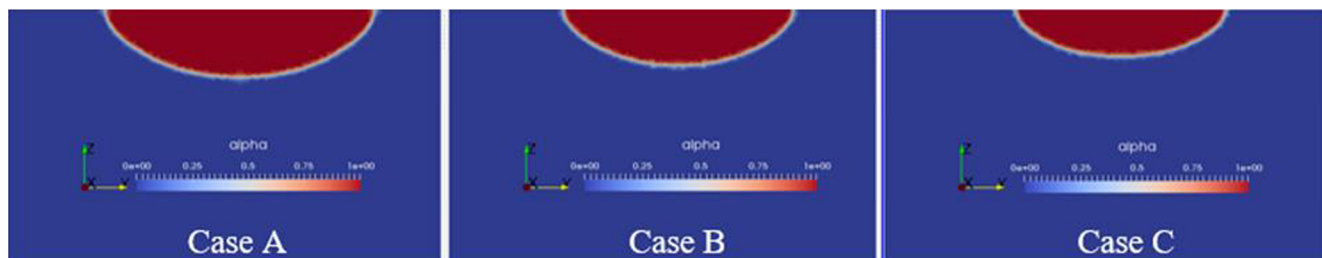

Fig. 5 Top view of the melt pool for each case

Fig. 6 Transverse cross-section view of the melt pool for each case

Table 3 Comparison of predicted versus measured values of melt-pool dimensions obtained from the experimental data [22] for the AMMT machine (dimensions in μm)

Power (W)	Velocity (m s^{-1})	Modeled values			Measured values (AMMT)		
		Length	Width	Depth	Length	Width	Depth
137.9	0.4	246	142	37.2	300	148	42.5
179.2	0.8	287	121	30.7	359	124	36.0
179.2	1.2	305	109	26.7	370	106	29.6

into the liquid cell, it remains liquid for the present time step. (4) This process of mapping the melt pool at each time step and the growth and solidification of CA cells is repeated for the entire length of each track.

AM-Bench Experimental Work

The AM-Bench experimental work was performed by NIST. The experiment was designed to isolate the effect of individual tracks printed on a bare plate of alloy IN625. The plate dimension is 24.82 mm × 24.08 mm × 3.18 mm [21]. The tracks were printed at the center of the plate and were separated by a distance of 0.5 mm. The plate geometry and the track positions are shown in Fig. 3. To avoid heat buildup, each track was printed at 5-min intervals. The nominal temperature of the base plate was 25 °C at the start of experiment. Three different process parameter sets were used to produce the tracks as shown in Table 2. The laser was a continuous-wave ytterbium fiber (Yb-fiber) laser with a wavelength of 1070 nm. The experimental work was performed using two machines, namely Additive Manufacturing Metrology Testbed (AMMT) and Commercial Built Machine (CBM) for which the laser spot sizes were 100 μm and 59 μm, respectively. The cooling rates were measured as shown in Fig. 4.

Results and Discussion

The results submitted by AO to NIST for the AMB2018 Test Series are shown in this section. Figure 5 shows the top view of the simulated melt pool which is shown for each case from Table 2. It can be observed that as the scan speed increases, the melt-pool shape elongates, while its width becomes

Table 4 Comparison of predicted versus measured values of melt-pool dimensions obtained from the experimental data [22] for the CBM machine (dimensions in μm)

Case	Modeled values			Measured values (CBM)		
	Length	Width	Depth	Length	Width	Depth
A	252	144	37.7	659	N/A	N/A
B	298	124	32.4	782	N/A	N/A
C	312	110	27.3	754	N/A	N/A

marginally narrower. Figure 6 shows a transverse cross section of the simulated melt pool at its widest location for each case. Similar to Fig. 5, the penetration of the melt pool in the substrate is a function of the combination of laser power and scan velocity, which correspond to different values of input energy density. The simulated melt-pool dimensions are summarized in Tables 3 and 4 along with their respective experimental results published by NIST [22]. Note only the melt-pool length was reported for the CBM machine.

The AMMT machine laser powers were revised at a later date by NIST to 137.9, 179.2, and 179.2 W for cases A, B, and C, respectively. Table 3 shows the melt-pool measurements obtained from the AMMT machine. The width and depth, as well as the length of the melt pool, are in agreement with the experiment results presented in Table 3. In general, the length of the melt pool is underpredicted by the model by ~ 23% for the AMMT machine. The length prediction errors are much larger for the CBM machine (Table 4). Even though the power and scan speed are the same for both machines, the input energy density for CBM is higher than AMMT because its spot size is significantly smaller. As a result, the phenomenology for the melt-pool thermal-fluid flow for the AMMT and CBM machines is likely to be different, resulting in different values for the melt-pool length. It is possible that the melt-pool model in AMP^2 simulations is more suited for the lower energy density values for AMMT. In any case, it is worthwhile to note that NIST has expressed that the melt-pool length measurements between the two machines differ significantly, and the source of this discrepancy is yet undetermined [22].

The cooling rates were calculated using the data from the predicted 3D temperature distributions and the equation given in Fig. 4. The results along with the experimental values are shown in Table 5. In general, the cooling rates are overpredicted. Figure 7 shows the temperature profiles along the scan track for all three cases, which were utilized for the cooling rate calculation. Ahead of the melting pool ($0 \mu m < x < 500 \mu m$), the temperature profiles are similar for all three cases. Within the melt pool, Fig. 8 shows that case A has a lower peak temperature than cases B and C. These values of peak temperature depend on the procedure utilized to model material vaporization. Behind the peak ($x < 0$), the cooling profiles are different for each case as shown in Fig. 9.

The denominator of the cooling rate calculation is the distance over which the temperature drops from 1290 to

Table 5 Comparison of predicted versus measured values of cooling rates obtained from the experimental data [22] for the CBM and AMMT machines

Case	Modeled cooling rate (K s^{-1})	Measured cooling rate (K s^{-1}) for CBM	Measured cooling rate (K s^{-1}) for AMMT
A	2.23E6	6.20E5	1.16E6
B	4.31E6	9.35E5	1.08E6
C	6.28E6	1.28E6	1.90E6

1000 °C, which corresponds to a region adjoining the melt-pool boundary since 1290 °C is solidus temperature for alloy IN625. The distance over which the temperature drops to 1000 °C is influenced by the melt-pool temperature distribution, which is governed by complex high-temperature phenomenology for which the material data is scant and approximate. The modeling of vaporization and melt-pool depression is particularly challenging in this regard. In addition, the measurement of temperature adjacent to the melt-pool boundary is also a difficult endeavor due to high scan velocity of the laser, the small size of the melt pool, and the sensor saturation caused by the high temperature melt pool. Thus, the discrepancy in the prediction of cooling rate can potentially be due to the limitations in the simulation as well as the measurement data.

The evolution of solidification grain structure was computed using the CA-Solidification software. An initial substrate was assumed to have a normal distribution of grain size with an average of 5 μm (Fig. 2). The CA grid was defined to have a resolution of 1 μm. The size of the substrate used by CA-Solidification for each case was chosen on the basis of their respective melt-pool dimensions. Specifically, the substrate dimensions were chosen to be sufficiently large in order to be able to attain a "quasi-steady state" for the size and shape of solidification grains as the melt pool passes through the substrate CA grid.

The 2D grain shapes and morphology were obtained from the 3D simulations. The transverse cross sections of the predicted grain shapes for each case are shown in Figs. 10, 11, and 12, which illustrate the predicted and measured
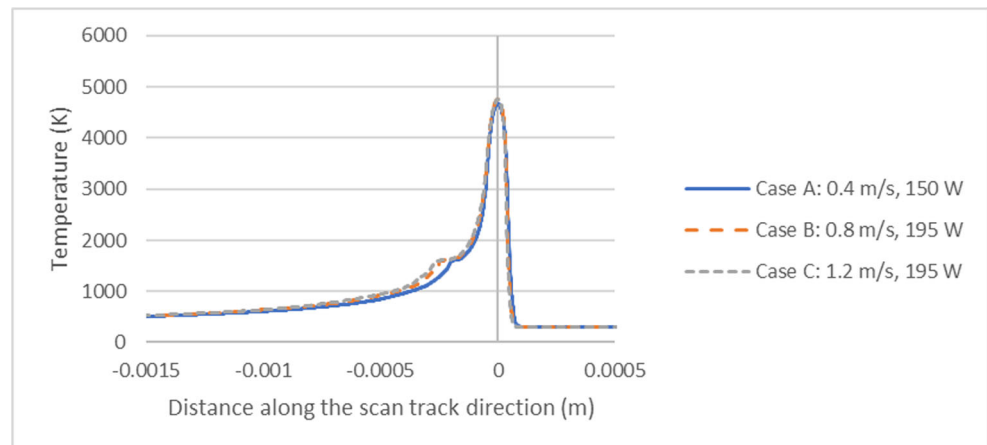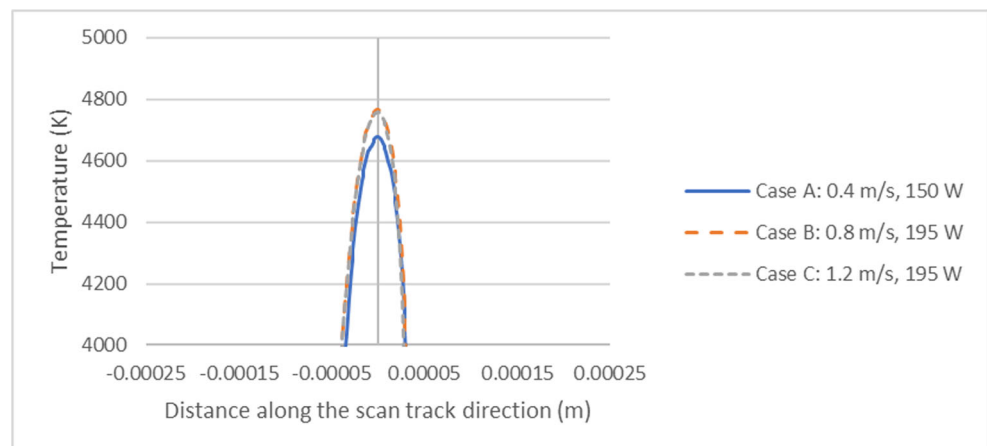
Fig. 7 Temperature (K) profile along the scan track direction for each case

Fig. 8 Close-up view on the peak temperatures

Fig. 9 Close-up view on the cooling region of the temperature profiles
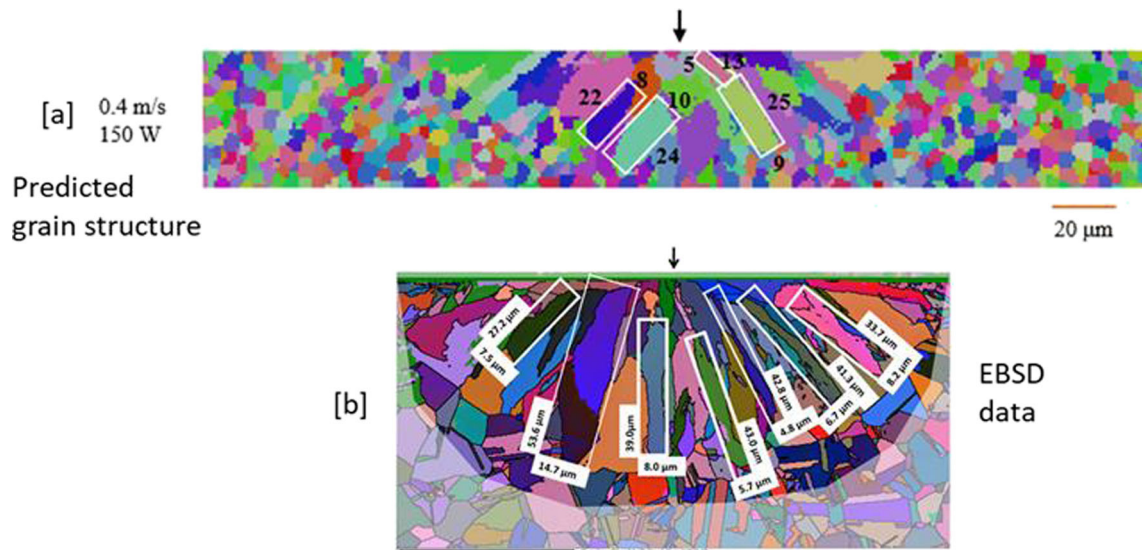

Fig. 10 Prediction of 2D grain structure (case A) with the numbers in grain length in micrometers

Fig. 11 Prediction of 2D grain structure (case B) with the numbers in grain length in micrometers
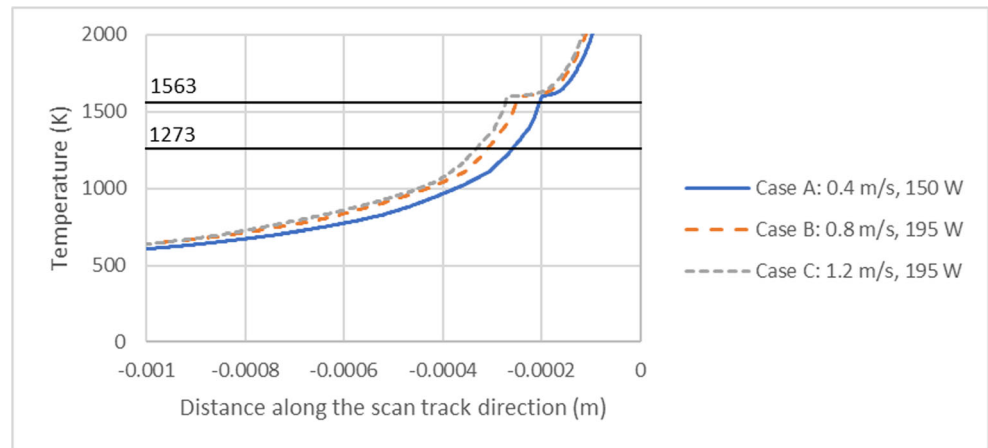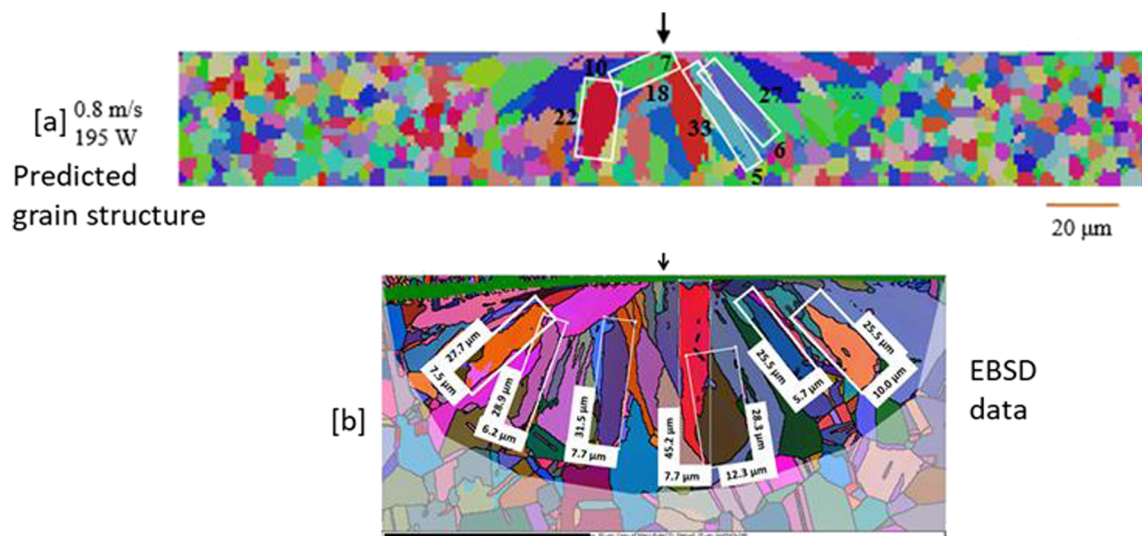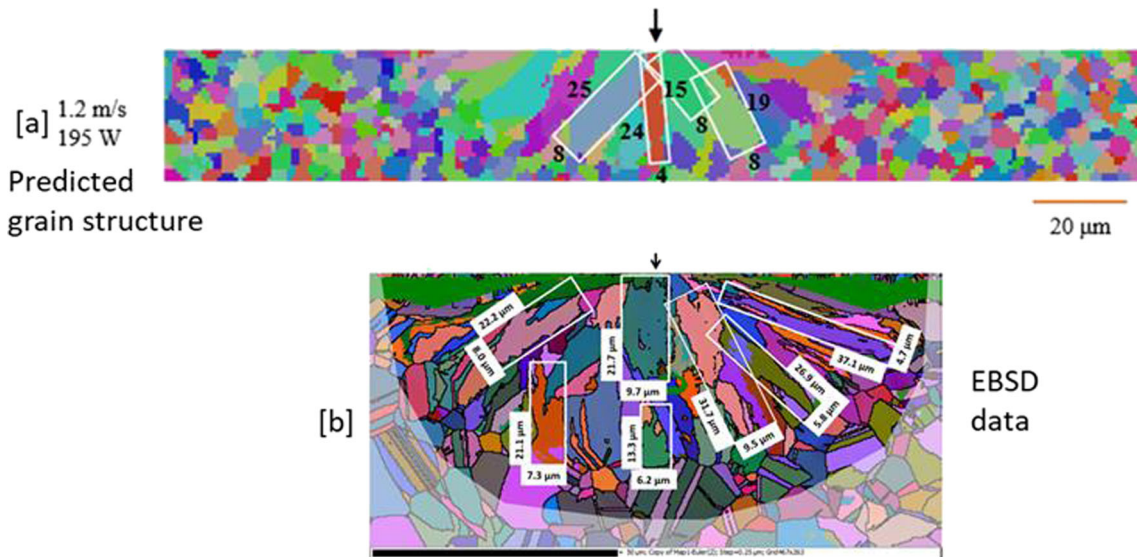
Fig. 12 Prediction of 2D grain structure (case C) with the numbers in grain length in micrometers

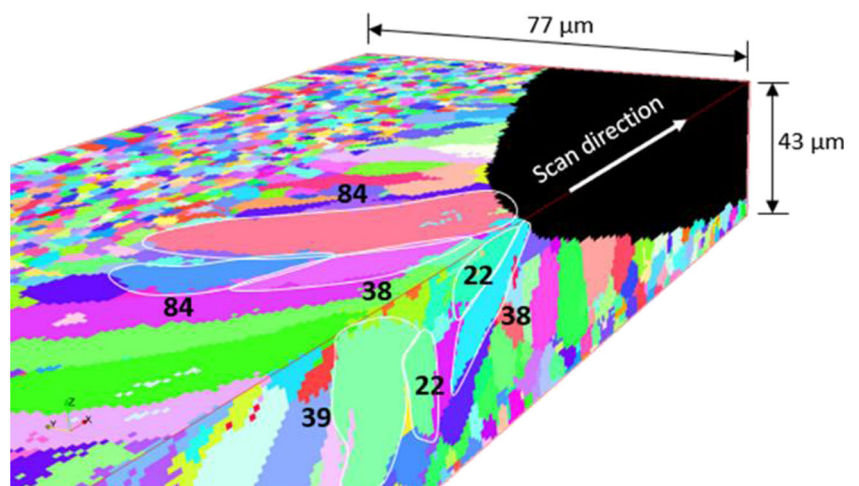**Fig. 13** Prediction of 3D grain structure (case A) with the numbers in grain length in micrometers

Fig. 14 Prediction of 3D grain structure (case B) with the numbers in grain length in micrometers
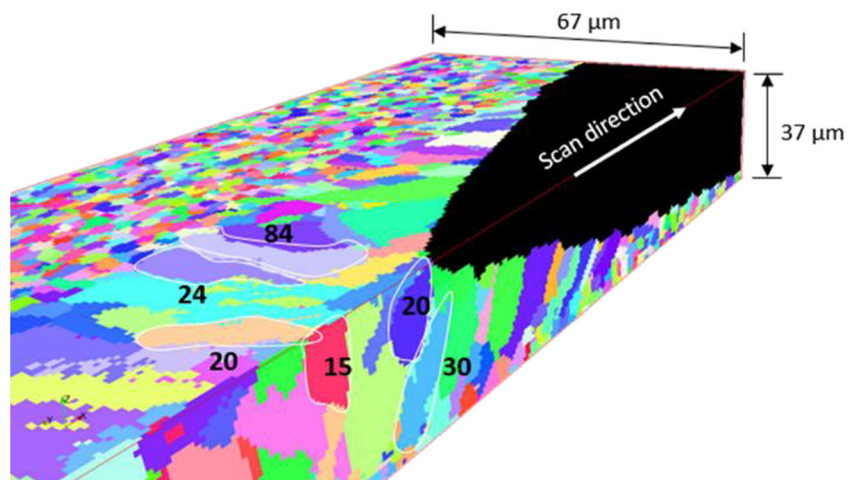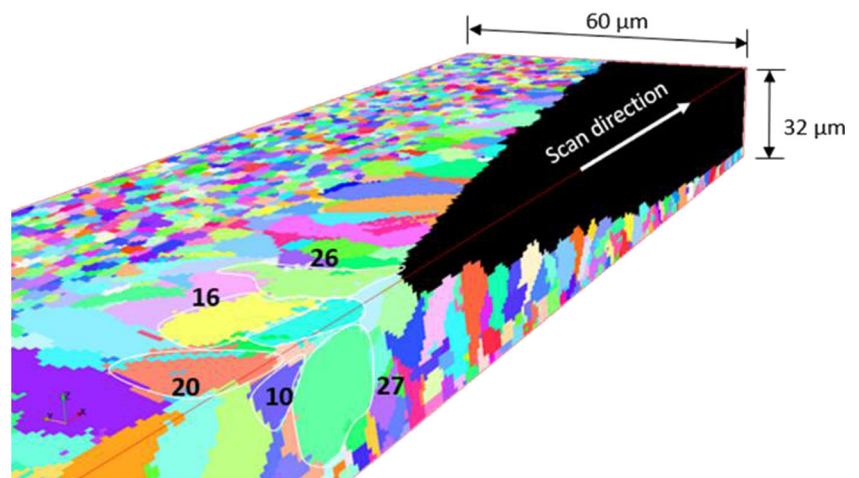
morphologies and growth directions of the grains. A few
grains are highlighted in each figure in order to identify their
respective size. The dimension of each highlighted grain in
micrometers is denoted with a number adjacent to that grain.
The cross sections were taken at 0 μm, − 6.3 μm, and
128.7 μm from the origin along the x-axis for cases A, B,
and C, respectively. The center of the melt pool is identified
with an arrow.

Case A seems to produce wider grains with a lower aspect
ratio than cases B and C. Case B seems to have produced the
most elongated grain shapes. As for case C, long grain shapes
were predicted with a slightly wider shape when compared
with case B's results. In all three cases, the growth direction
of the grains is toward the center of the melt pool.

For the prediction of 3D structure, the CA-Solidification
procedure was utilized to generate a 3D prediction of the so-
lidification grain structure. Figures 13, 14, and 15 show the
3D grain structure for cases A, B, and C, respectively. These
figures show only half the width of the substrate in order to
look at a longitudinal cross section along the x-axis. A few
grains are also highlighted in each figure. Each identified
grain is denoted with its approximate length in micrometers.
The black region is the current melt-pool position.

Conclusions

The results presented in this paper comprise an outcome of a
blind test of the predictive capability of AM simulations and
can be considered akin to a single data point toward an assess-
ment of a TML to reduce the testing required to develop a
material or process in the industry [2]. The results are present-
ed for four of the six challenges of the AM-Bench Test Series
AMB2018-02. The melt-pool geometry, cooling rate, grain
shapes, and 3D structures were obtained using the AMP^2 soft-
ware developed by AO. The melt-pool geometry and cooling

rate were predicted using a thermal-CFD solution of the melt-
pool. The predictions of grain shapes and 3D structure were
obtained by using the thermal predictions from the melt-pool
simulation as input to a CA algorithm.

The prediction of melt-pool width and depth provided good
agreement with the AM-Bench experiment data. The melt-
pool length was underpredicted for both AMMT and CBM
machines. The prediction error was < 25% for the AMMT
where the melt-pool lengths were shorter and > 100% for
CBM where the melt-pool lengths were over twice as large.
This discrepancy in the melt-pool length measurements is yet
undetermined. The cooling rates were overpredicted. These
under-/overpredictions are potentially a result of limitations
of the simulation model as well as the challenges in collecting
experimental data for a small fast-moving melt pool that con-
tains very high-temperature material, which cools rapidly as
the melt pool moves away.

The patterns of solidification microstructure were ob-
served to be consistent with the electron backscatter dif-
fraction (EBSD) image provided in the NIST description
of the benchmark challenge. The grain size predicted by
the CA simulation was measured by processing its output
image data. Typical length and width for grains in the
transverse cross section were observed to be ∼ 7 μm and
∼ 22 μm, respectively. The grains at the top surface of the
substrate were observed to be wider and longer than the
grains in the transverse cross section. Based on the com-
parison of the predictions with the EBSD data, AO re-
ceived a second-place award for Challenge AMB2018-
02-GS for predicting the grain structure within three sin-
gle laser tracks on a bare IN625 plate [23].

Compliance with Ethical Standards

Conflict of Interest The authors declare that they have no conflict of
interest.

Appendix 1: Related Work on the Prediction of Melt-Pool Length

In this attachment, we compare Applied Optimization, Inc.'s melt-pool simulation results for melt-pool length with the experimental data published by Heigel and Lane [13]. Their work reports the melt-pool length during a single scan track on a bare plate of IN625 for seven different cases with a laser power ranging from 49 to 195 W and a scan speed between 200 and 800 mm s^{-1}. The plate is 3.2 mm thick with a width and length of 25.4 mm. The initial temperature of the plate and the ambient temperature are both 30 °C. The laser used is an Yb-fiber laser with a maximum power of 200 W, a spot size of 100 μm, and an estimated absorption of 0.51. The experimental data for the corresponding results for the melt-pool length predictions are given in Table 6.

Table 6 Comparison of melt-pool length prediction with experimental data [13]

Case	Power (W)	Speed (mm s^{-1})	Experimental melt-pool length (m)	ParaGen prediction of melt-pool length (m)	Error (%)
1	49	200	1.71E−04	1.81E−04	5.89
2	122	200	5.19E−04	2.62E−04	− 49.44
3	122	500	3.61E−04	2.65E−04	− 26.56
4	122	800	3.15E−04	2.69E−04	− 14.60
5	195	200	8.24E−04	2.96E−04	− 64.10
6	195	500	9.03E−04	3.11E−04	− 65.58
7	195	800	8.13E−04	3.16E−04	− 61.11

Appendix 2: Related Work on the Prediction of Melt-Pool Width and Depth

Criales et al. [14] published data on the modeling of multi-track processing for laser powder bed fusion of alloy IN625. This process is different from the AM-Bench experiments because the laser follows a zig-zag scan path. Applied Optimization, Inc. predicted the melt-pool width and depth for a total of 14 cases with two predictions each for type I and II tracks. Type I simulations accounted for heat buildup where type II simulations assumed no heat buildup (i.e., substrate at initial temperature). The laser power ranged from 169 to 195 W, and the scan speed ranged from 0.725 to 0.875 m/s. For type II simulations, the initial temperature of the plate with powder and the ambient temperature were both 80 °C. For type I, the initial temperature of the plate with powder was obtained from type II simulations. The location of the measured temperature is two hatch distances behind the melt pool and one hatch distance over. The laser used is an Yb-fiber laser with a maximum power of 200 W, a spot size of 100 μm, and an estimated absorption of 0.51. The powder has an estimated average diameter of 30.6 μm with a packing density of 0.5. The bed drop is 20 μm.

Tables 7 and 8 present the predicted width and depth for type I melt pool, and Tables 9 and 10 depict the predicted width and depth for type II melt pool. The melt-pool width prediction is in good agreement with the experimental data for type II melt pool (average error of 4%). As for the type I width and type II depth, the predicted values have an average error of 18%. Type I depth has an average error of 24%.

Table 7 Type I predicted width result comparison with experimental data [14]

Case	P (W)	v (mm s^{-1})	h (mm)	Experimental data		ParaGen	Error (%)
				Type I width (μm)	SD	Type I width (μm)	
1	169	875	0.10	134	12	109.9	18
2	195	875	0.10	170	25	122.5	28
3	182	875	0.09	149	17	115.3	23
4	182	725	0.11	153	25	123.7	19
5	195	800	0.11	143	13	123.8	13
6	182	725	0.09	134	18	139.0	4
7	182	800	0.10	132	11	113.8	14
8	195	725	0.10	152	13	138.5	9
9	182	875	0.11	134	13	112.0	16
10	169	725	0.10	159	13	120.9	24
11	169	800	0.09	154	14	119.2	23
12	169	800	0.11	150	28	113.7	24
13	195	800	0.09	149	15	135.6	9
14	195	800	0.10	155	11	128.9	17

Table 8 Type I predicted depth result comparison with experimental data [14]

Case	P (W)	v (mm s^{-1})	h (mm)	Experimental data		ParaGen	Error (%)
				Type I depth (μm)	SD	Type I depth (μm)	
1	169	875	0.10	35	6	32.4	7
2	195	875	0.10	49	7	29.9	39
3	182	875	0.09	45	7	33.7	25
4	182	725	0.11	48	8	35.8	25
5	195	800	0.11	44	7	33.7	23
6	182	725	0.09	45	7	38.5	14
7	182	800	0.10	44	7	32.6	26
8	195	725	0.10	52	18	38.6	26
9	182	875	0.11	47	7	33.7	28
10	169	725	0.10	51	8	36.2	29
11	169	800	0.09	47	8	35.5	24
12	169	800	0.11	43	6	33.1	23
13	195	800	0.09	49	7	37.4	24
14	195	800	0.10	50	6	39.8	20

Table 9 Type II predicted width result comparison with experimental data [14]

Case	P (W)	v (mm s^{-1})	h (mm)	Experimental data		ParaGen	Error (%)
				Type II width (μm)	SD	Type II width (μm)	
1	169	875	0.10	92	9	102.2	11
2	195	875	0.10	111	7	111.7	1
3	182	875	0.09	101	16	104.3	3
4	182	725	0.11	107	12	115.2	8
5	195	800	0.11	109	9	112.4	3
6	182	725	0.09	113	11	115.2	2
7	182	800	0.10	109	10	106.5	2
8	195	725	0.10	114	11	115.4	1
9	182	875	0.11	110	15	104.3	5
10	169	725	0.10	106	8	108.9	3
11	169	800	0.09	107	9	100.1	6
12	169	800	0.11	96	11	100.1	4
13	195	800	0.09	103	16	112.4	9
14	195	800	0.10	112	15	112.4	0

Table 10 Type II predicted depth result comparison with experimental data [14]

Case	P (W)	v (mm s^{-1})	h (mm)	Experimental data		ParaGen	Error (%)
				Type II depth (μm)	SD	Type II depth (μm)	
1	169	875	0.10	31	5	31.3	1
2	195	875	0.10	46	8	33.5	27
3	182	875	0.09	38	5	31.8	16
4	182	725	0.11	39	9	31.6	19
5	195	800	0.11	42	7	29.3	30
6	182	725	0.09	36	10	31.6	12
7	182	800	0.10	38	6	38.5	1
8	195	725	0.10	42	10	31.6	25
9	182	875	0.11	32	7	31.8	1
10	169	725	0.10	42	6	32.9	22
11	169	800	0.09	45	9	30.0	33
12	169	800	0.11	33	6	30.0	9
13	195	800	0.09	39	12	29.3	25
14	195	800	0.10	41	7	29.3	29

References

1. O'Connell PJ (2012) Systems engineering applications for small business innovative research (SBR) projects. Air Force Institute of Technology, Wright-Patterson Air Force Base, OH. https://scholar.afit.edu/cgi/viewcontent.cgi?article=2284&context=etd. Accessed 31 Dec 2018

2. Cowles B, Backman D, Dutton R (2012) Verification and validation of ICME methods and models for aerospace applications. Integr Mater Manuf Innov 1(1):2

3. AMP^2. Applied Optimization, Fairborn, OH. http://appliedo.com/amp2/. Accessed 15 Jan 2019

4. DebRoy T, Wei HL, Zuback JS, Mukherjee T, Elmer JW, Milewski JO, Beese AM, Wilson-Heid A, De A, Zhang W (2018) Additive manufacturing of metallic components–process, structure and properties. Prog Mater Sci 92:112–224

5. Knapp GL, Mukherjee T, Zuback JS, Wei HL, Palmer TA, De A, DebRoy T (2017) Building blocks for a digital twin of additive manufacturing. Acta Mater 135:390–399

6. Gan Z, Liu H, Li S, He X, Yu G (2017) Modeling of thermal behavior and mass transport in multi-layer laser additive manufacturing of Ni-based alloy on cast iron. Int J Heat Mass Transf 111:709–722

7. Gan Z, Yu G, He X, Li S (2017) Surface-active element transport and its effect on liquid metal flow in laser-assisted additive manufacturing. Int Commun Heat Mass Transfer 86:206–214

8. Shamsaei N, Yadollahi A, Bian L, Thompson SM (2015) An overview of direct laser deposition for additive manufacturing; part II: mechanical behavior, process parameter optimization and control. Addit Manuf 8:12–35

9. Foster SJ, Carver K, Dinwiddie RB, List F, Unocic KA, Chaudhary A, Babu SS (2018) Process-defect-structure-property correlations during laser powder bed fusion of alloy 718: role of in situ and ex situ characterizations. Metall Mater Trans A 49(11):5775–5798

10. Gan Z, Lian Y, Lin SE, Jones KK, Liu WK, Wagner GJ (2019) Benchmark study of thermal behavior, surface topography, and dendritic microstructure in selective laser melting of Inconel 625. Integr Mater Manufact Innov:1–16. https://doi.org/10.1007/s40192-019-00130-x

11. Vincent TJ, Rumpfkeil MP, Chaudhary A (2018) Numerical simulation of molten flow in directed energy deposition using an iterative geometry technique. Lasers Manuf Mater Process 5(2):113–132

12. Ribic BD (2011) Modeling of plasma and thermo-fluid transport in hybrid welding. Pennsylvania State University. https://etda.libraries.psu.edu/files/final_submissions/654. Accessed 15 Jan 2019

13. Heigel JC, Lane BM (2017) Measurement of the melt pool length during single scan tracks in a commercial laser powder bed fusion process. Addit Manuf Mater 2. https://doi.org/10.1115/MSEC2017-2942

14. Criales LE, Arısoy YM, Lane B, Moylan S, Donmez A, Özel T (2017) Predictive modeling and optimization of multi-track processing for laser powder bed fusion of nickel alloy 625. Addit Manuf 13:14–36. https://doi.org/10.1016/j.addma.2016.11.004

15. Capriccioli A, Frosi P (2009) Multipurpose ANSYS FE procedure for welding processes simulation. Fusion Eng Des 84(2–6):546–553. https://doi.org/10.1016/j.fusengdes.2009.01.039

16. Criales LE, Arısoy YM, Özel T (2016) Sensitivity analysis of material and process parameters in finite element modeling of selective laser melting of Inconel 625. Int J Adv Manuf Technol 86(9–12):2653–2666. https://doi.org/10.1007/s00170-015-8329-y

17. Cagran C, Reschab H, Tanzer R, Schützenhöfer W, Graf A, Pottlacher G (2009) Normal spectral emissivity of the industrially used alloys NiCr20TiAl, Inconel 718, X2CrNiMo18-14-3, and another austenitic steel at 684.5 nm. Int J Thermophys 30(4):1300–1309. https://doi.org/10.1007/s10765-009-0604-4

18. Montgomery C, Beuth J, Sheridan L, Klingbeil N (2015) Process mapping of Inconel 625 in laser powder bed additive manufacturing. Solid Free Fabr Symp:1195–1204

19. DREAM.3D. http://dream3d.bluequartz.net/. Accessed 09 May 2018

20. Rai A, Helmer H, Körner C (2017) Simulation of grain structure evolution during powder bed based additive manufacturing. Addit Manuf 13:124–134. https://doi.org/10.1016/j.addma.2016.10.007

21. NIST (2018) Additive manufacturing benchmark test series (AM-BENCH) AMB2018-02 description. https://www.nist.gov/ambench/amb2018-02-description. Accessed 15 Jan 2019

22. NIST (2018) CHAL-AMB2018-02-MP-length. https://www.nist.gov/ambench/chal-amb2018-02-mp-length. Accessed 15 Jan 2019

23. NIST (2018) Additive manufacturing benchmark test series (AM-BENCH) awards. https://www.nist.gov/ambench/awards. Accessed 15 Jan 2019